Tuning of dielectric properties of SrTiO₃ in the terahertz range

V. Skoromets,[1] F. Kadlec,[1] C. Kadlec,[1] H. Němec,[1] I. Rychetsky,[1] G. Panaitov,[2] V. Müller,[3] D. Fattakhova-Rohlfing,[3]
P. Moch,[4] and P. Kužel[1,*]

[1]*Institute of Physics, Academy of Sciences of the Czech Republic, Na Slovance 2, CZ-182 21 Prague 8, Czech Republic*
[2]*Institute of Bio and Nanosystems, Research Centre Jülich, D-52425 Jülich, Germany and*
JARA–Fundamentals of Future Information Technology
[3]*Department of Chemistry and Biochemistry, University of Munich (LMU), Butenandtstrasse 5-13, D-81377 Munich, Germany*
[4]*Laboratoire des Sciences des Procédés et des Matériaux (LSPM) (CNRS-UPR 3407), Université Paris 13, 99 Avenue J.-B. Clément, F-93430
Villetaneuse, France*

Tuning of the dielectric permittivity spectra of strontium titanate (SrTiO₃) single crystals in an external electric field is investigated between 90 and 300 K by means of terahertz time-domain spectroscopy. Application of the electric bias leads to an appreciable tuning of the permittivity observed up to room temperature both in the parallel and perpendicular directions to the bias field. The observed behavior is interpreted in terms of soft-mode hardening due to the anharmonic character of its potential. No additional low-frequency relaxation mode was observed. A weak temperature dependence of the anharmonic coefficients was found in agreement with previously published low-temperature data.

PACS number(s): 77.22.Ch

I. INTRODUCTION

The terahertz (THz) frequency region has become extensively exploited during the past two decades. Nowadays THz technology finds applications in medical, space, and defense industries, to cite only the most prominent ones. The investigation of tunable properties of various materials and structures plays an important role in the development of components enabling active control of the propagation of THz radiation.

From the point of view of fundamental research the THz and sub-THz regions—covering ∼0.2–3 THz—are crucial for the investigation of structural phase transitions of solids; in particular, deep insight can be acquired into the mechanisms of ferroelectric phase transitions.[1] Two limiting cases of structural phase transitions are often distinguished: displacive and order-disorder types. These are often associated with characteristic excitations, a soft phonon mode (displacive case) and a relaxation-type central mode (order-disorder case), respectively. In real materials these two excitations often coexist, in some cases they are even mutually coupled, and they occur frequently in the THz spectral range. Their polar character allows a straightforward detection in THz transmission measurements.

In the vicinity of a phase transition, ferroelectric materials are characterized by a fine compensation of various microscopic forces.[2] Then, anharmonic properties of the crystalline lattice potential often play a crucial role and can be easily experimentally accessed.[3] Under suitable conditions a high and tunable permittivity accompanied by reasonably low dielectric losses can be achieved in the THz spectral range.[4] This opens a large potential for a number of tunable applications of such materials, e.g., by means of an external low-frequency electric field.

Strontium titanate (STO) is an incipient ferroelectric material. The low-frequency dielectric behavior of STO single crystals is fully controlled by soft-mode dynamics; at the same time the compound remains paraelectric down to the lowest temperatures due to quantum fluctuations. The frequency of the soft mode in STO decreases upon cooling. According to the Lyddane-Sachs-Teller relation,[5] this leads to an increase of the permittivity in the THz and sub-THz ranges and, consequently, to an increase of its electric-field tunability.

The electric-field tuning of the dielectric properties of STO single crystals and unstrained films was previously extensively studied in view of its applications in microwave tunable devices. However, these studies have been mostly limited to low temperatures (20–90 K) and to low frequencies (at GHz range and below).[6–8] It was commonly accepted that the dielectric properties of STO single crystals are not tunable above ∼100 K.

An increased room-temperature tunability of STO-based structures in the microwave and THz ranges was achieved by chemical substitution of strontium by barium (Ba$_x$Sr$_{1−x}$TiO₃ solid solutions),[4] or by tensile strain introduced during the epitaxial growth of STO thin films on appropriate substrates.[9] This last possibility has been intensely studied during the past years in a series of STO/DyScO₃ thin films and heterostructures.[10–14] A general model of the soft-mode behavior in strained epitaxial STO films has been proposed.[13] It describes dielectric spectra of the films in a very broad range of temperatures (20–300 K) and applied fields: The tunable effective permittivity of the heterostructures and films is given by a strongly anharmonic THz soft phonon mode which couples to a low-frequency overdamped excitation (at ∼200 GHz).

Only preliminary results obtained by THz spectroscopy were previously reported about the soft-mode behavior under the electric field in a bulk STO.[15] From the study of Raman spectra below 80 K under an applied bias, Fleury and Worlock[16] estimated the anharmonic parameters of the soft-mode potential. Our own unpublished Brillouin scattering measurements show that the acoustic modes are insensitive to an applied electric field above 90 K. To the best of our knowledge, no observation of the tunability of STO single crystals at room temperature has been reported up to now. In

this paper we use time-domain THz spectroscopy to demonstrate and characterize the electric-field-tuning capabilities of STO single crystals in the THz spectral range within a broad interval of temperatures (90–300 K). The electric-field-induced soft-mode hardening is quantified both for the parallel and perpendicular directions with respect to the electric bias.

II. THEORETICAL DESCRIPTION

We base our description on the Landau-Devonshire theory, which provides a direct evaluation of the dielectric response of ferroelectrics. As expected for a displacive incipient ferroelectric, STO is characterized by a strong transverse soft phonon mode which accounts for more than 95% of its dc permittivity value. The Helmholtz free-energy density F is here expanded in a power series with respect to the components P_i of the macroscopic polarization vector. This polarization is associated with the soft-mode eigenvector characterized by a relative displacement of the oxygen octahedron with respect to the central Ti ion. In the paraelectric state of STO the spontaneous part of the polarization vanishes. We are then left with a bias-field-induced dc or low-frequency term ΔP_i and with a small dynamic term $P_{i,\mathrm{dyn}}$ driven by a weak probing field: $P_i = \Delta P_i + P_{i,\mathrm{dyn}}$. The weakness of the probing field ensures that nonlinear effects arise only from ΔP_i ($\Delta P_i \gg P_{i,\mathrm{dyn}}$). The allowed terms in the Helmholtz free-energy density up to the fourth order of the power series in the cubic paraelectric phase of STO read[4,16]

$$F(T) = \tfrac{1}{2}\alpha\left(P_x^2 + P_y^2 + P_z^2\right) + \tfrac{1}{4}\beta_\parallel\left(P_x^4 + P_y^4 + P_z^4\right) + \tfrac{1}{2}\beta_\perp\left(P_x^2 P_y^2 + P_y^2 P_z^2 + P_z^2 P_x^2\right),\tag{1}$$

where $\beta_\parallel$ and $\beta_\perp$ characterize the anharmonicity of the soft mode. This describes the tetragonal symmetry of the structure induced by the applied bias. The coefficient describing the harmonic part of the potential can be written as[12]

$$\alpha = \frac{\omega_0^2}{f\,\varepsilon_{\mathrm{vac}}},\tag{2}$$

where ω_0 is the soft-mode bare frequency, f is its oscillator strength, and $\varepsilon_{\mathrm{vac}}$ is the vacuum permittivity. The relation between an external electric field with components E_i and the induced polarization is given by a dielectric equation of state

$$E_i = \frac{\partial F}{\partial P_i},\tag{3}$$

e.g., for the z component

$$E_z = \alpha P_z + \beta_\parallel P_z^3 + \beta_\perp P_z\left(P_x^2 + P_y^2\right).\tag{4}$$

For the other two components of the field analogous equations are found.

Within the linear approximation, the polarization related to the soft mode is equal to $P_i = \varepsilon_{\mathrm{vac}}\delta\varepsilon E_i$, where $\delta\varepsilon$ is the harmonic contribution of the soft mode to the permittivity:

$$\delta\varepsilon = \frac{1}{\alpha\varepsilon_{\mathrm{vac}}} = \frac{f}{\omega_0^2}.\tag{5}$$
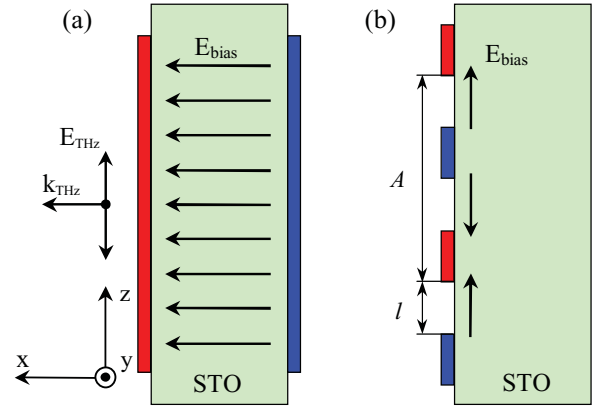

FIG. 1. (Color online) Schematic illustration of the two experimental geometries used: (a) Perpendicular geometry; nanocrystalline tin oxide electrodes; and (b) parallel geometry; the bias is applied by using interdigitated metallic electrodes. $A = 40\ \mu$m: period of the electrode structure; $l = 15\ \mu$m: distance between electrode fingers.

The oscillator strength f is, as a rule, temperature independent; the permittivity value in the sub-THz range then crucially depends on the soft-mode frequency.

The electric-field tunability is related to the anharmonicity of the Helmholtz potential, as we show below. In the coordinate system we use (shown in Fig. 1), the probing THz electric field is parallel to the z direction, therefore, we wish to evaluate the component ε_{zz} of the dielectric permittivity as a function of a parallel [E_z, Fig. 1(b)] and of a perpendicular [E_x, Fig. 1(a)] bias electric field. In these configurations P_y vanishes and one finds

$$\varepsilon_{zz} = \frac{1}{\varepsilon_{\mathrm{vac}}}\frac{\partial P_z}{\partial E_z} + \varepsilon_\infty$$
$$\approx \left[\frac{1}{\delta\varepsilon} + 3\beta_\parallel\varepsilon_{\mathrm{vac}}(\Delta P_z)^2 + \beta_\perp\varepsilon_{\mathrm{vac}}(\Delta P_x)^2\right]^{-1} + \varepsilon_\infty;\tag{6}$$

here ε_∞ is a cumulative contribution to the permittivity caused by higher-frequency excitations such as hard phonons and electrons.

In the absence of bias field the polarization ΔP_i vanishes and $\varepsilon_{zz}(T) = \delta\varepsilon(T) + \varepsilon_\infty \equiv \varepsilon_0(T)$; here the temperature dependence of the permittivity is essentially given by the temperature dependence of the soft-mode frequency. If an external bias is applied, we need to evaluate the induced polarizations ΔP_x and ΔP_z; to this aim, we use the lowest-order terms of the power expansion of Eq. (4):

$$P_z \approx \frac{1}{\alpha}E_z - \frac{\beta_\parallel}{\alpha^4}E_z^3 - \frac{\beta_\perp}{\alpha^4}E_z E_x^2,\tag{7a}$$

$$P_x \approx \frac{1}{\alpha}E_x - \frac{\beta_\parallel}{\alpha^4}E_x^3 - \frac{\beta_\perp}{\alpha^4}E_x E_z^2.\tag{7b}$$

We now discuss the two geometries depicted in Fig. 1. (i) In the perpendicular geometry [Fig. 1(a)] $E_x = E_{\mathrm{bias}}$ and $E_z = E_{\mathrm{THz}}$. The linear response to the THz field then reads

$$P_{z,\mathrm{dyn}} \approx \left(\frac{1}{\alpha} - \frac{\beta_\perp}{\alpha^4}E_{\mathrm{bias}}^2\right)E_{\mathrm{THz}}\tag{8}$$

and

$$\varepsilon_{zz}\left(E_{\text{bias}} \parallel x\right) = \left[\frac{1}{\delta\varepsilon} + \frac{\beta_\perp f^2 \varepsilon_{\text{vac}}^3 E_{\text{bias}}^2}{\omega_0^4} + \cdots\right]^{-1} + \varepsilon_\infty. \quad (9)$$

In other words, application of an external bias $E_{\text{bias}} \parallel x$ leads to a change of the soft-mode potential due to its anharmonic character and we observe a field-induced soft-mode hardening, which can be deduced by using Eqs. (5) and (6) or (9):

$$\omega_0^2(E_{\text{bias}} \parallel x) = \omega_0^2 \left[1 + \frac{\beta_\perp \varepsilon_{\text{vac}} f}{\omega_0^2}(\Delta P_x)^2\right]$$

$$\approx \omega_0^2 \left[1 + \beta_\perp \left(\frac{\varepsilon_{\text{vac}} f}{\omega_0^2}\right)^3 E_{\text{bias}}^2\right]. \quad (10)$$

(ii) In the parallel geometry, as a first approximation [shown in Fig. 1(b)], we assume that $E_x = 0$ and $E_z = E_{\text{bias}} + E_{\text{THz}}$ and

$$P_{z,\text{dyn}} \approx \left(\frac{1}{\alpha} - 3\frac{\beta_\parallel}{\alpha^4} E_{\text{bias}}^2\right) E_{\text{THz}}. \quad (11)$$

The expression for the permittivity then reads

$$\varepsilon_{zz}\left(E_{\text{bias}} \parallel z\right) = \left[\frac{1}{\delta\varepsilon} + \frac{3\beta_\parallel f^2 \varepsilon_{\text{vac}}^3 E_{\text{bias}}^2}{\omega_0^4} + \cdots\right]^{-1} + \varepsilon_\infty$$

$$(12)$$

and

$$\omega_0^2(E_{\text{bias}} \parallel z) = \omega_0^2 \left[1 + \frac{3\beta_\parallel \varepsilon_{\text{vac}} f}{\omega_0^2}(\Delta P_z)^2\right]$$

$$\approx \omega_0^2 \left[1 + 3\beta_\parallel \left(\frac{\varepsilon_{\text{vac}} f}{\omega_0^2}\right)^3 E_{\text{bias}}^2\right]. \quad (13)$$

In reality, the bias field in the parallel geometry is highly inhomogeneous and it rapidly decays along x inside STO. In this sense only a thin STO layer is influenced by the applied field and, for the purpose of evaluating the THz transmission data, we wish to determine the effective thickness d_E of this layer and an effective value of the applied field E_{bias} which would then be assumed homogeneous within d_E. We performed electrostatic simulations[17] to determine the distribution of the bias field close to the interdigitated electrode structure for this geometry [Fig. 2(a)]. Both the z and x components of the field are nonzero and highly inhomogeneous along x and z [$E_z(x,z)$ and $E_x(x,z)$]. The variation along x of their averaged squared values $(E_{z,\text{avg}})^2$ and $(E_{x,\text{avg}})^2$ is shown in Fig. 2(b): Each plotted value is averaged over a 1-μm-thick layer parallel to the interface, e.g., the first plotted values of $(E_{z,\text{avg}})^2$ and $(E_{x,\text{avg}})^2$ are each obtained as an average value of the appropriate component over one period of the electrode structure along z and between 0 and 1 μm depth along x.

A natural choice for the z component of the effective field would be $E_{z,\text{bias}} = U_{\text{bias}}/l$, where U_{bias} is the applied bias voltage and $l = 15$ μm is the distance between the electrode fingers. For this component we found

$$\int_0^\infty (E_{z,\text{avg}})^2 dx = (E_{z,\text{bias}})^2 d_E \approx (E_{z,\text{max}})^2 d_E, \quad (14)$$
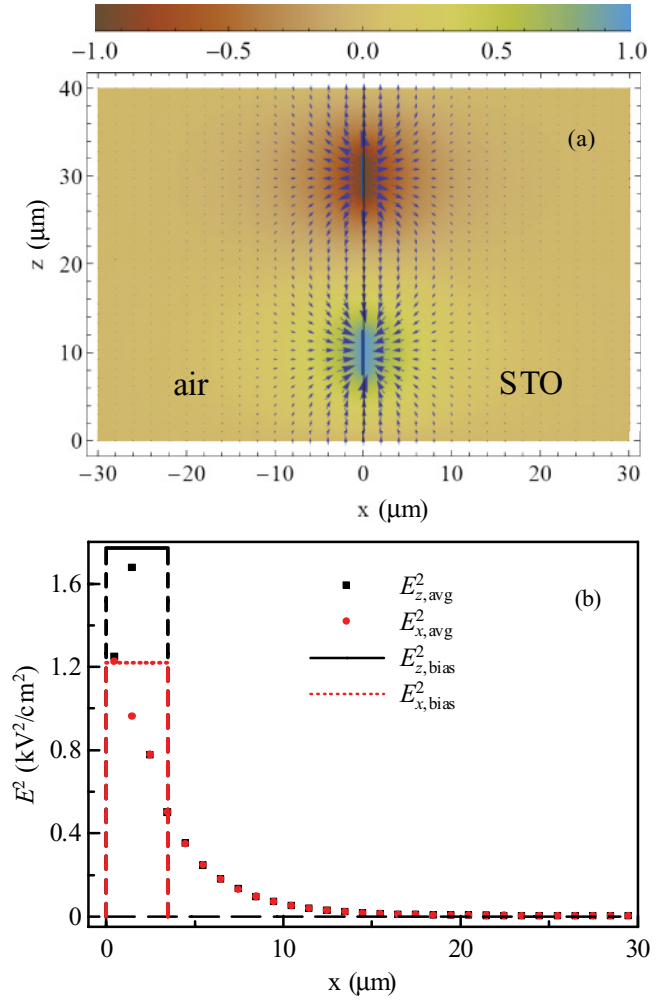

FIG. 2. (Color online) Electrostatic simulation of the electric-field distribution near the air-STO interface ($x = 0$). (a) Arrows: electric-field distribution; colors: electrostatic potential distribution. (b) Squared value of the bias field components $E_{z,\text{avg}}$ and $E_{x,\text{avg}}$ averaged over 1-μm-thick slices in the x direction parallel to the surface. The simulation is done for an electrostatic potential of ± 1 V on the electrodes.

and similarly for the x component we obtain

$$\int_0^\infty (E_{x,\text{avg}})^2 dx \approx (E_{x,\text{max}})^2 d_E, \quad (15)$$

where $(E_{i,\text{max}})^2$ ($i = x,z$) is the maximum averaged squared-field value (see Fig. 2) and the penetration depth $d_E \approx 3.5$ μm is the same for both components. It is then natural to define $E_{x,\text{bias}} = E_{x,\text{max}}$ for the purposes of evaluation of our experimental data.

The soft-mode frequency in the parallel geometry then depends on both the x and z components of the bias field and, combining (10) and (13) we obtain

$$\omega_0^2(E_{x,\text{bias}}, E_{z,\text{bias}})$$

$$\approx \omega_0^2 \left[1 + 3\beta_\parallel \left(\frac{\varepsilon_{\text{vac}} f}{\omega_0^2}\right)^3 E_{z,\text{bias}}^2 + \beta_\perp \left(\frac{\varepsilon_{\text{vac}} f}{\omega_0^2}\right)^3 E_{x,\text{bias}}^2\right].$$

$$(16)$$

Finally, we come to the conclusion that in the parallel geometry both the z and x components of the bias field influence the soft-mode potential. Nevertheless, the z component of the field is dominant and the x component induces only a small correction of the soft-mode frequency. Indeed, a multiplication factor of 3 is lacking in the $\beta_\perp$ term in Eq. (16), and moreover, as can be seen in Fig. 2(b), the x component of the bias field is smaller than the z component one.

Note that measurements performed in the two experimental geometries allow us to evaluate the two different anharmonic coefficients of the soft-mode potential $\beta_\parallel$ and $\beta_\perp$. These coefficients were previously found to have similar values of the order of 10^{10} JC^{-4}m^5 at low temperatures.[16]

For both geometries, the dynamical response in the THz range then can be simply described by a harmonic oscillator formula, where the soft-mode frequency is tunable by the external bias:

$$\varepsilon_{zz}(\omega; T, E_{\text{bias}}) = \frac{f}{\omega_0^2(T, E_{\text{bias}}) - \omega^2 - i\omega\Gamma(T)} + \varepsilon_\infty.$$
(17)

The soft-mode damping Γ is slightly temperature dependent[18] and, in principle, it can be also weakly electric-field dependent, although field dependence of the damping coefficient has not been found in the strained STO thin films.[10–13]

A ferroelastic cubic-to-tetragonal phase transition (PT) is known to occur at 105 K in STO crystals. In the low-temperature ferroelastic phase the (cubic T_{1u}) ferroelectric soft mode splits into a doubly degenerated E_u mode and a higher-frequency A_{2u} mode, as reported, e.g., in a hyper-Raman study by Yamanaka *et al.*[18] This means that the linear dielectric properties of STO become anisotropic; however, as the soft-mode splitting is continuous, this anisotropy is quite small at temperatures close to the PT. For instance, at 90 K the frequency splitting is of $\sim$0.9 cm^{-1}, i.e., of $\sim$2% of the mean frequency value. In this case the anisotropy of the permittivity is only $\sim$4%.[19]

In the THz transmission spectra the soft-mode splitting cannot be directly observed, since even the thinnest samples used are completely opaque above $\sim$1 THz. In principle, the studied samples consist of a distribution of optically anisotropic parts forming a polydomain composite. However, down to $\sim$90 K this local optical anisotropy remains weak and the experimental data represent an average dielectric response of such a composite. The measured field-induced soft-mode hardening can then be understood as an average hardening of the two split soft-mode components.

III. EXPERIMENTAL DETAILS

Several series of experiments were done and numerous spectra were acquired and analyzed in the frame of this work. All the experimental spectra were measured using a custom-made time-domain terahertz spectrometer (described in detail in Ref. 20) fitted with a helium flow cryostat (Optistat, Oxford instruments). The investigated STO crystals were purchased from Crystal GmbH and thinned down by mechanical polishing to the thickness of 50 or 100 μm. The dimensions of the studied samples were $10 \times 10 \times 0.1$

and $10 \times 10 \times 0.05$ mm^3. Chemical etching, which, unlike mechanical polishing, is known to produce no residual stress,[7] could not be used because it leads to a corrugated surface,[21] unsuitable for subsequent electrode deposition.

In order to realize experimentally both parallel and perpendicular geometries (Fig. 1), we deposited two different electrode structures on the samples. In the first series of samples an interdigitated electrode structure was deposited on a single side [Fig. 1(b)]. This structure was prepared by magnetron sputtering deposition of an intermediate 20-nm Nb adhesion layer and of a 300-nm-thick Au layer; subsequently, the electrodes were formed using a standard lift-off photolithography. The resulting electrodes consisted of 5-μm-wide metal stripes separated by 15-μm-wide gaps. The total area covered by the electrode structure was $\sim$6 $\times$ 6 mm^2. These electrodes allow application of an in-plane bias field, i.e., enable experiments in the parallel geometry; they are transparent for the THz radiation when the electric-field vector is perpendicular to the metallic stripes.

Measurement in the perpendicular geometry requires deposition of electrodes on both sides of the platelets [Fig. 1(a)]. We used nanocrystalline antimony-doped tin oxide films which combine a sufficient electric conductivity and transparency in the THz range. The synthesis of Sb-doped tin oxide nanoparticles was published elsewhere.[22] For electrode fabrication, the dried nanoparticles (0.2 g) were dispersed in tetrahydrofuran (4 mL) containing one drop of concentrated HCl. The obtained transparent colloidal solutions were deposited on the substrates by spin coating and calcined afterward at 500°C. The area covered with the electrodes was $\sim$8 $\times$ 8 mm^2 in this case. Finally, an additional sample was prepared with an interdigitated electrode structure on one side and a nanocrystalline tin oxide thin film deposited on the other side. This served to check the consistency of the experimental results obtained in both geometries using the same STO crystal.

The experiments were performed in the transmission geometry using an optical cryostat equipped with electrical connections for applying the bias; the area on the sample probed by the THz beam was defined by a metallic aperture with a diameter of 5–8 mm. This makes the experiments in the perpendicular geometry more complicated. In order to achieve good electrical insulation of the sample from the cryostat, an additional dielectric spacer had to be inserted between the metallic aperture and the sample. Extreme experimental care was taken to avoid artifacts in the measured signal: These are caused by a partial reflection of the THz pulse on the front sample surface which is subsequently diffracted on the edges of the aperture. This parasitic signal was tunable by the applied electric bias and it came to the detector as a slightly delayed weak signal pulse echo stretched in time.

We used a high-voltage source to apply the bias fields with the possibility of monitoring the current in order to keep the samples far from dielectric breakdown. For each sample a series of wave forms, i.e., transmitted time-domain THz field $E(t)$ [Fig. 3(a)], was measured in a repeated sequence. Each sequence was started by a reference measurement (zero-bias field) and continued by increasing stepwise the bias voltage during the returns of the optical delay line. After a scan with the maximum bias voltage the sequence was restarted and the whole procedure was repeated many times in order to
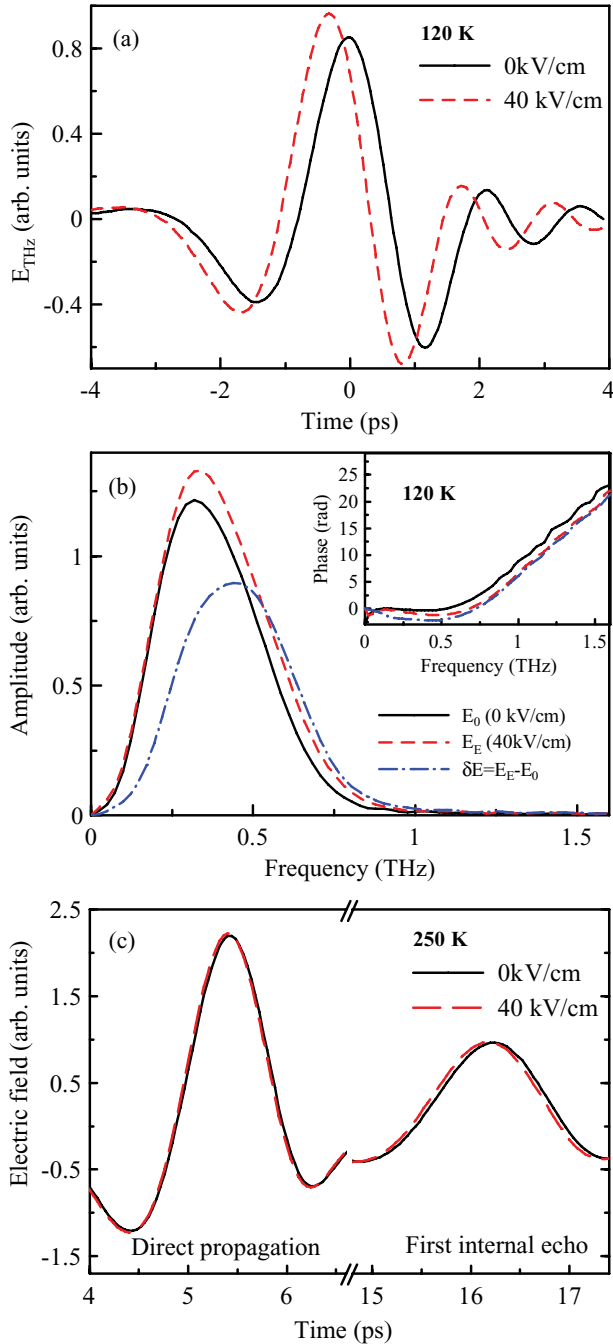
FIG. 3. (Color online) Experimental wave forms and spectra obtained with a 100-μm-thick STO crystal in the perpendicular geometry: (a) Time-domain wave forms, 120 K; (b) Fourier transformations of the wave forms, 120 K; (c) time-domain wave form measured at 250 K with the first echo; here the field-induced tuning is visible for the echo (its displacement to shorter time delays with applied voltage corresponds to a field-induced reduction of the permittivity).

improve the signal-to-noise ratio. This procedure minimized the influence of possible long-term drifts of the laser beam. The data acquisition at each temperature and for approximately six to eight values of the bias field lasted ∼3–4 h.

The THz dielectric spectra of unbiased STO (we denote the permittivity ε_0 and the refractive index N_0) were determined and published previously.[15] The spectra of the biased samples N_E were determined numerically as a root of a complex equation for each spectral component:

$$\frac{T(\omega; N_E)}{T(\omega; N_0)} = \frac{T_E(\omega)}{T_0(\omega)}. \tag{18}$$

The spectra T_E and T_0 on the right-hand side are the measured complex transmission functions with and without bias, respectively. The left-hand side of Eq. (18) contains the theoretical expressions for the transmittance; these expressions stem from the Fresnel formulas and depend on the experimental geometry used.

For experiments in the perpendicular geometry the field distribution inside the sample is homogeneous, and, consequently, the complex refractive index under bias N_E is also homogeneous. The samples are optically thick in the THz frequency range, which means that we may take advantage of the time-domain windowing procedure.[23] Due to Fabry-Pérot reflections inside the sample, the signal wave form consists of a series of echoes well separated in time. The experimental wave form is truncated in such a way that the studied part of the signal corresponds to the mth echo which leaves the sample after $2m$ internal reflections. This partial wave form is then transformed to the frequency space by Fourier transformation. For the mth echo we obtain the complex transmission function as follows:

$$T^{m\text{th}}(\omega; N) = \frac{4N}{(N+1)^2} \exp(i\omega Nd/c) \left[\frac{(N-1)}{(N+1)}\right]^{2m}$$
$$\times \exp(2im\omega Nd/c), \tag{19}$$

where the complex refractive index N ($\equiv N_0$ or N_E) is a function of frequency $N(\omega) = n(\omega) + i\kappa(\omega)$, d is the thickness of the sample, and c is the light velocity in vacuum.

At low temperature the dielectric spectra were obtained from a direct pass ($m = 0$). When the temperature is increased, the sample becomes more transparent and is less tunable at the same time. In this case it is advantageous to perform the calculation for a higher-order echo ($m = 1$ or 2) for which the corresponding transmitted signal is still sufficiently high but more influenced by the change of the refractive index. For example, the first echo undergoes three passes through the sample while the directly passing beam undergoes a single one. This procedure increases the sensitivity of the measurement [see Fig. 3(c)].

For experiments in the parallel geometry, Fig. 2(b) illustrates the approximation we use in the data evaluation procedure. We consider a fraction of the sample under bias as a thin film with a homogeneous refractive index N_E and thickness d_E while the remaining bulk part was treated as a substrate with the refractive index N_0. The ratio of the transmission functions for the whole sample with and without bias then reads

$$\frac{T(\omega; N_E)}{T(\omega; N_0)} = \frac{2N_E(N_0 + 1)\exp(i\omega(N_E - N_0)d_E/c)}{(1 + N_E)(N_E + N_0) + (1 - N_E)(N_E - N_0)\exp(2i\omega N_E d_E/c)}. \tag{20}$$
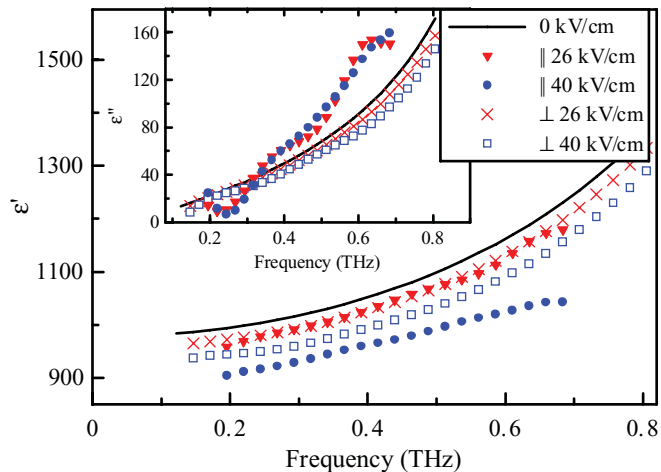
FIG. 4. (Color online) Dielectric permittivity of a 100-μm-thick STO crystal at 120 K. Unbiased permittivity (solid line) is approximated using an underdamped harmonic oscillator model (Ref. 15). The electric-field-induced permittivity was calculated from the experimental wave forms. Full symbols represent results of the tuning using the parallel geometry; crosses and empty symbols represent results obtained in the perpendicular geometry.

Finally, we compared the sensitivity of the measurements in the parallel and perpendicular geometries. Assuming identical values for the parallel and perpendicular anharmonic terms, a comparison of Eqs. (10) and (16) shows that the soft-mode frequency (and the permittivity) should depend more steeply on the bias field in the parallel geometry. Also, for applied identical voltages, the bias electric field close to the electrodes is substantially higher in the parallel geometry, leading to much higher field-induced effects in this part of the sample. However, the perpendicular geometry allows one to induce a homogeneous change of the permittivity in the whole volume of the sample while in the parallel geometry only a 3.5-μm-thick layer is affected by the bias field. The THz pulse then acquires useful information only when it propagates through this thin layer and afterward it just suffers an unwanted absorption in the rest of the sample. Taking these facts into account, we conclude that the perpendicular arrangement provides a larger sensitivity and a better accuracy for the measurement of the field-induced effects than the parallel one.

IV. EXPERIMENTAL RESULTS AND DISCUSSION

Examples of raw experimental data are shown in Fig. 3. At 120 K the soft-mode frequency is as low as 1.5 THz; as a result, the sample is relatively opaque while its tunability is high [Figs. 3(a) and 3(b)]. Close to room temperature the soft-mode frequency rises above 2.4 THz and the sample becomes much more transparent; at the same time the tunability is significantly reduced compared to low temperatures [see data at 250 K shown in Fig. 3(c)]. Note that at higher temperatures (250 and 300 K) the field-induced changes of the permittivity were determined from the transmittance calculated using the first THz echo. In Fig. 3(c) the small field-induced contribution is visible as an advance of the first echo obtained under bias compared to that obtained without bias (i.e., $N_E < N_0$). This

approach allowed us to quantify the tunability of STO up to room temperature.

The calculated permittivity spectra at 120 K under the bias for both geometries are shown in Fig. 4. The real part of the permittivity is decreasing when increasing the bias in the whole experimentally accessible frequency range for both geometries; as shown in the theoretical section, this is a signature of soft-mode hardening. For the data obtained in the perpendicular geometry, we note that the shape of the calculated dielectric spectra remains unchanged within the experimental uncertainty; this means that soft-mode damping does not change significantly with applied bias. The data obtained in the parallel geometry exhibit a slightly higher tunability of the real permittivity; the losses also increase under bias, as the damping of the soft mode increases. This is probably related to a broadening induced by the inhomogeneous distribution of the applied field.

We did not observe any measurable hysteresis of the electric-field-induced properties at 90 K, in agreement with the low-temperature and low-frequency data reported in Ref. 24. This justifies our description presented at the end of Sec. II of the tetragonal sample as an approximately cubic medium.

A. Perpendicular geometry

Selected experimental spectra of the field-induced tunability obtained in the perpendicular geometry are shown in Fig. 5. We characterize the tunability by relative changes of the real and imaginary dielectric functions $\Delta\varepsilon'/\varepsilon_0'$ and $\Delta\varepsilon''/\varepsilon_0'$, where $\Delta\varepsilon'$ and $\Delta\varepsilon''$ are the variations upon the applied field of the real and imaginary parts of the permittivity, and ε_0' is the real permittivity without an external bias.

Relative field-induced changes of the dielectric function for several temperatures under the same electric bias field of 40 kV/cm are shown in Figs. 5(a) and 5(b). The field-induced tunability of the permittivity is increasing upon cooling and toward higher frequencies at all temperatures. In Fig. 5 the lines represent fits of the experimental data by an underdamped harmonic oscillator model given by Eq. (17). We found that the oscillator strength f and the high-frequency permittivity ε_∞ do not change with temperature and electric field. Consequently, we used previously published literature values[15] which were fixed for all our fits in this paper. In addition, the values of the temperature-dependent soft-mode frequency and damping in unbiased STO were also taken from the literature.[15] The only fitting parameters are thus the soft-mode frequency and damping in biased STO. Our fit reveals that the soft-mode frequency constitutes the crucial parameter which describes nearly entirely the field-induced changes observed in the spectra. The soft-mode damping does not vary substantially with the field and its variation has only a minor impact on the fit. A decrease of the real part of the permittivity induced by a field of 40 kV/cm is ~6 % at 120 K. The change of its imaginary part is smaller but its frequency dependence becomes steeper with decreasing temperature. This is consistent with an increased tunability of STO at lower temperatures: The soft mode softens with decreasing temperature, leading to larger anharmonic effects upon any applied bias field. In Figs. 5(c) and 5(d) we show analogous results obtained at 150 K for several external bias fields.
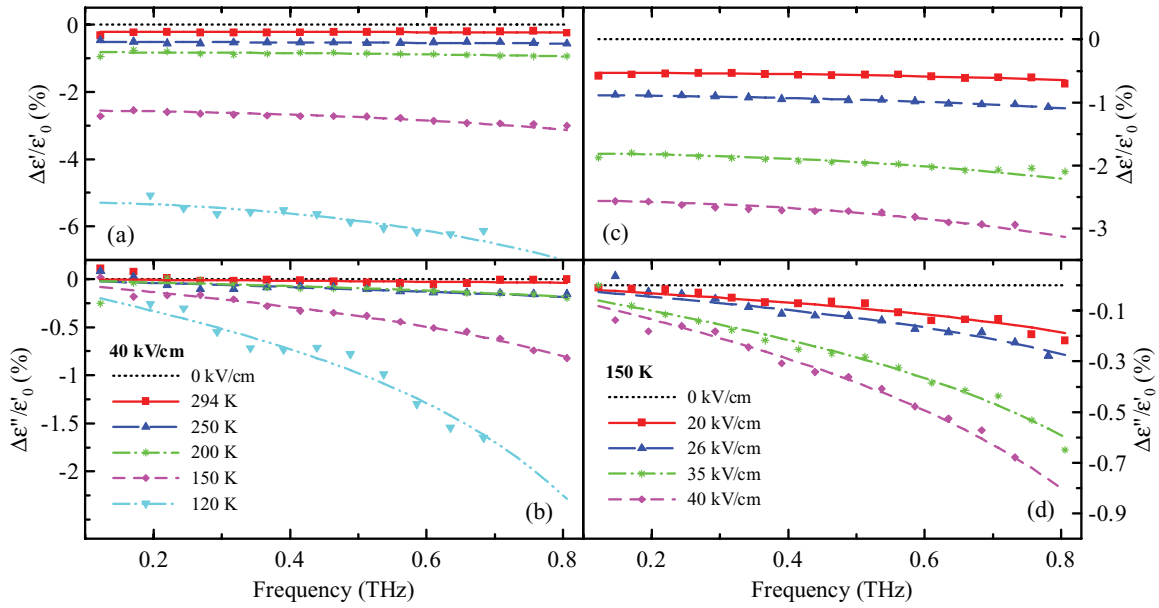
FIG. 5. (Color online) Relative field-induced changes in the complex dielectric function obtained for the perpendicular geometry. (a) and (b) $E_{bias} = 40$ kV/cm, varying T; (c) and (d) $T = 150$ K, varying the bias field. Symbols: Experimental data. Lines: Fits by an underdamped harmonic oscillator.

The behavior of the real and imaginary parts of the field-induced changes is in agreement with the picture of soft-mode hardening with increasing temperature and electric bias.

The tuning of the soft-mode frequency is shown in Fig. 6; it is expressed as the difference between the soft-mode frequency with the field on and off: $\Delta\omega_0(E_{bias}) = \omega_0(E_{bias}) - \omega_0$. The values $\omega_0(E_{bias})$ were obtained by fitting the entire set of complex permittivity spectra with the harmonic oscillator model. The curves at each temperature were fitted with an expression derived from formula (10), which is valid for a reasonably weak field:

$$\Delta\omega_0(E_{bias}) \approx \omega_0 \left[\sqrt{1 + \beta_\perp \left(\varepsilon_{vac} f / \omega_0^2\right)^3 E_{bias}^2} - 1 \right]. \quad (21)$$
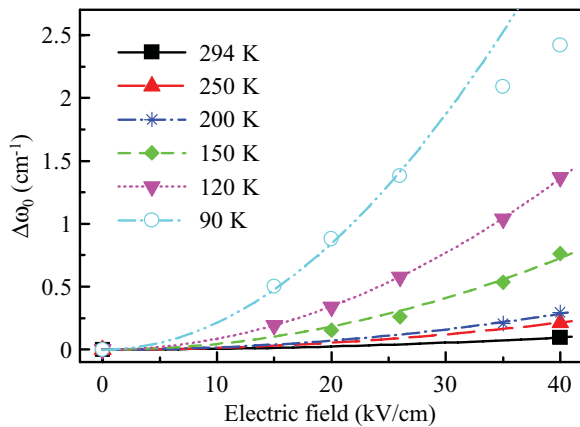

FIG. 6. (Color online) Electric-field-induced hardening of the soft mode in the perpendicular geometry at several temperatures. The symbols represent the fits of the experimental spectra using a harmonic oscillator model (17); the lines represent fits of the soft-mode behavior at each temperature by using Eq. (21).

Here we are left with a single fitting parameter, the anharmonic coefficient $\beta_\perp$. The largest field-induced change in the soft-mode frequency under a maximum bias field of 40 kV/cm occurs at $T = 90$ K; it amounts to 2.4 cm^{-1}, which represents $\sim$6% of the frequency of the soft mode. The field-induced changes of the permittivity exceed 15% in this case, and the observed saturation of the soft-mode hardening in Fig. 6 can be explained by higher-order terms in E_{bias}, which were neglected in Eq. (21). For this reason the two results obtained at $T = 90$ K for the highest-bias fields were not taken into account in this fitting.

B. Parallel geometry

Experimental spectra of the field-induced tunability obtained in the parallel geometry are illustrated in Fig. 7. As already pointed out, the experimental sensitivity in this case is lower than in the perpendicular geometry. This can be seen namely in Figs. 7(b) and 7(d) for the imaginary part of the permittivity, where the noise is considerably larger, thus providing less satisfactory fits. Nevertheless, the change of the real part of the dielectric function at 40 kV/cm and 120 K is larger ($\sim$10 %) than the value found in the perpendicular geometry under the same applied field and at the same temperature.

The distribution of the applied bias field is highly inhomogeneous in this geometry, as illustrated in Fig. 2(a). This should result in an inhomogeneous broadening of the soft-mode spectral line. Consequently, the best fits are obtained for a slightly increased value of the damping parameter Γ of the soft mode compared to its zero-field value: E.g., at 120 K the damping value at high fields increases by up to 65% compared to zero field [$\Gamma(E_{bias} = 0) = 8$ cm^{-1}];[15] close to room temperature this increase is not observed. This effect can be also observed in Figs. 7(b) and 7(d). For higher
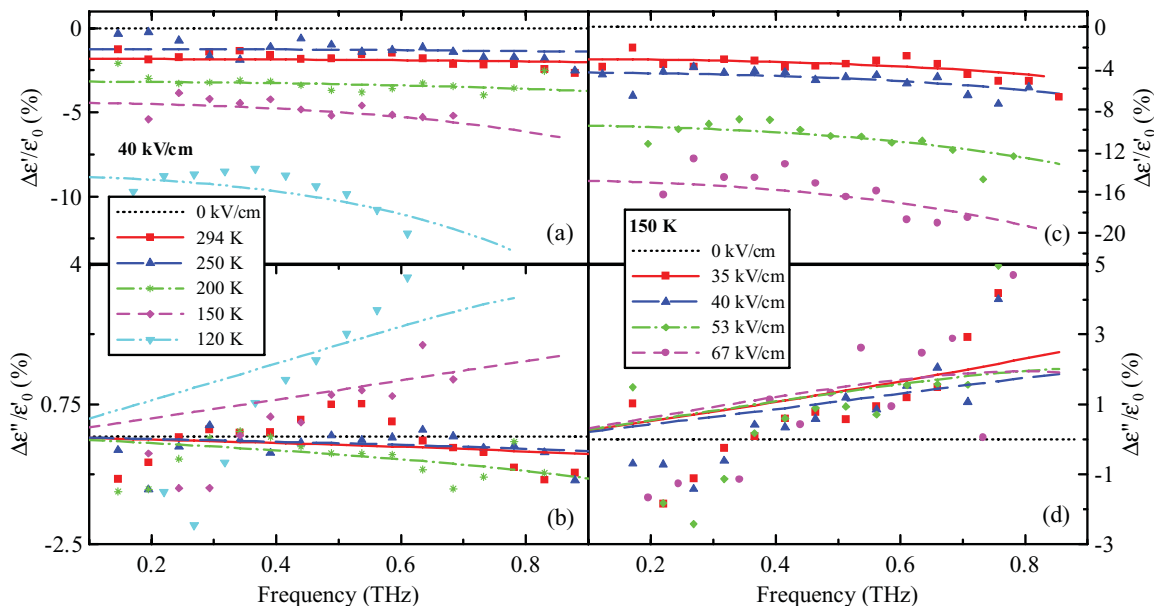
FIG. 7. (Color online) Relative field-induced changes in the complex dielectric function in the parallel geometry. (a) and (b) $E_{\rm bias} = 40\,{\rm kV/cm}$, varying T; (c) and (d) $T = 150\,{\rm K}$, varying the bias field. Symbols: Experimental data. Lines: Fits by an underdamped harmonic oscillator.

temperatures ($T \geqslant 200\,{\rm K}$) $\Delta\varepsilon''(\omega) < 0$ as it was similarly found for the perpendicular geometry, and this reflects soft-mode hardening. In contrast, for low temperatures $\Delta\varepsilon''(\omega) > 0$ due to a significant increase of soft-mode damping.

The soft-mode frequency tuning by the electric field in the parallel geometry is shown in Fig. 8. The largest field-induced change in the soft-mode frequency under a maximum bias field of $67\,{\rm kV/cm}$ and at $T = 90\,{\rm K}$ is $10.5\,{\rm cm^{-1}}$ which corresponds to $\sim 27\%$ of the soft-mode frequency without bias. The fits were performed by using an expression derived from (16) in which the presence of both the z and x components of the bias is taken into account:

$$\Delta\omega_0(E_{\rm bias}) \approx \omega_0\left[\sqrt{1 + 3\beta_\parallel\left(\varepsilon_{\rm vac}f/\omega_0^2\right)^3 E_{z,{\rm bias}}^2 + \beta_\perp\left(\varepsilon_{\rm vac}f/\omega_0^2\right)^3 E_{x,{\rm bias}}^2} - 1\right]. \tag{22}$$

Again, the only fitted parameter is the anharmonic coefficient $\beta_\parallel$, while $\beta_\perp$ is already known from the experiments
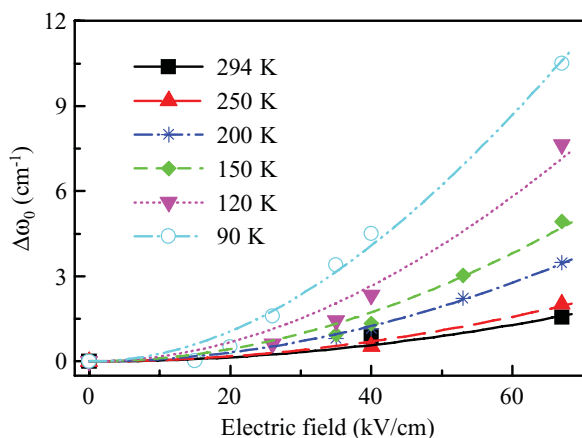

FIG. 8. (Color online) Electric-field-induced hardening of the soft mode in the parallel geometry at several temperatures. Symbols are obtained from the fits of the experimental spectra by a harmonic oscillator model (17); lines represent fits of the soft-mode behavior at each temperature by using Eq. (22).

using the perpendicular geometry. A relation between values of the bias field components $E_{z,{\rm bias}}$ and $E_{x,{\rm bias}}$ is obtained from the calculation of the electric-field distribution pattern shown in Fig. 2.

C. Nonlinear potential

In Fig. 9 the temperature dependences of $\beta_\parallel$ and $\beta_\perp$ are shown together with data by Christen *et al.*,[6] which was obtained from the measurements in the microwave spectral range. According to our data, the anharmonic parameter $\beta_\parallel$ monotonically decreases with cooling while Christen *et al.*, at lower temperatures (below 80 K), reported its increase with cooling. Note, however, that a ferroelastic antiferrodistortive phase transition occurs at 105 K in STO; the change in the slope of temperature variation of the anharmonic parameters in this region may indicate an influence of the phase transition on the soft-mode potential.

The values of the anharmonic parameter $\beta_\parallel$ are slightly lower than those of $\beta_\perp$ at temperatures below 200 K, while they show both the same order of magnitude as the values reported in Ref. 6. We have to keep in mind that our values of $\beta_\parallel$ include a large experimental error due to the highly inhomogeneous
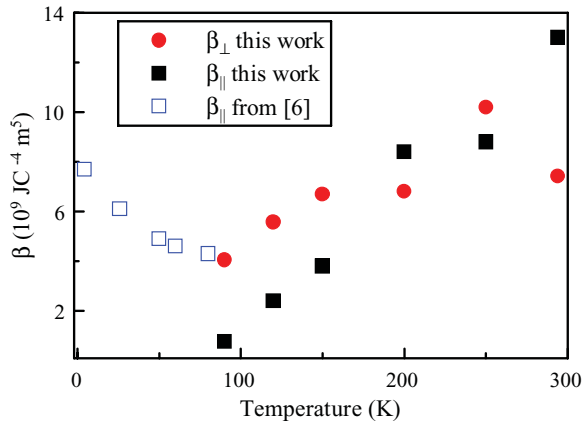
FIG. 9. (Color online) Resulting anharmonic parameters $\beta_\perp$ and $\beta_\parallel$ as functions of temperature (solid symbols) and $\beta_\parallel$ taken from Ref. 6 (open symbols).

character of the applied field in the parallel geometry and within this accuracy we may state that $\beta_\parallel \approx \beta_\perp$. The soft-mode potential then possesses an approximately spherical symmetry up to the fourth order of the power expansion. Our values are also consistent with those estimated previously by Fleury and Worlock[16] from the Raman spectra for temperatures below 80 K. The authors also concluded that $\beta_\parallel \approx \beta_\perp$ below 80 K. Finally, let us note that low-frequency experiments interpreted within a frame of the transverse Ising model[24] yield a comparable value of the third-order nonlinear susceptibility $\chi^{(3)} = \beta_\parallel \chi^4 \varepsilon_{\mathrm{vac}}^3$ (where χ is the linear susceptibility).

Our experimental results and their fits strongly indicate that the electric-field tuning of STO single crystals is entirely due to the anharmonic potential of the soft mode. This was observed in the whole investigated range of temperatures and of applied fields. The soft-mode dynamics determines the dielectric spectra in the THz and sub-THz range and no sign of additional relaxation mode was observed. This contrasts with the properties of strained STO films where the ferroelectric phase transition, which occurs close to room temperature, is connected to a soft mode that is strongly coupled to a relaxation mode at ~200 GHz.[13]

V. CONCLUSION

We investigated the electric-field-induced tunability of the dielectric properties of bulk strontium titanate crystals using terahertz time-domain spectroscopy in a broad temperature range. Two kinds of electrode structures deposited on the samples enabled the investigation of field-induced tuning in two different orientations of the probing field with respect to the bias. For both experimental geometries the theoretical description based on the Landau-Devonshire theory is presented. The variation of the dielectric properties is fully described by a hardening of the soft mode under the external electric field. An appreciable tunability is revealed up to room temperature. The results of this paper provide a reference point for further development of tunable structures (such as photonic crystals and/or metamaterials), which could be controlled by an external voltage.

*kuzelp@fzu.cz

[1] J. Hlinka, T. Ostapchuk, D. Nuzhnyy, J. Petzelt, P. Kužel, C. Kadlec, P. Vaněk, I. Ponomareva, and L. Bellaiche, Phys. Rev. Lett. **101**, 167402 (2008).

[2] M. E. Lines and A. M. Glass, *Principles and Applications of Ferroelectrics and Related Materials* (Oxford University Press, Oxford, UK, 1997).

[3] Y. Ishibashi, Ferroelectrics **195**, 81 (1997).

[4] A. K. Tagantsev, V. O. Sherman, K. F. Astafiev, J. Venkatesh, and N. Setter, J. Electroceram. **11**, 5 (2003).

[5] R. H. Lyddane, R. G. Sachs, and E. Teller, Phys. Rev. **59**, 673 (1941).

[6] H.-M. Christen, J. Mannhart, E. J. Williams, and Ch. Gerber, Phys. Rev. B **49**, 12095 (1994).

[7] J. Dec, W. Kleemann, and B. Westwanski, J. Phys. Condens. Matter **11**, L379 (1999).

[8] A. Eriksson, A. Deleniv, and S. Gevorgian, J. Appl. Phys. **93**, 2848 (2003).

[9] J. H. Haeni, P. Irvin, W. Chang, R. Uecker, P. Reiche, Y. L. Li, S. Choudhury, W. Tian, M. E. Hawley, B. Craigo, A. K. Tagantsev, X. Q. Pan, S. K. Streiffer, L. Q. Chen, S. W. Kirchoefer, J. Levy, and D. G. Schlom, Nature (London) **430**, 758 (2004).

[10] P. Kužel, F. Kadlec, J. Petzelt, J. Schubert, and G. Panaitov, Appl. Phys. Lett. **91**, 232911 (2007).

[11] P. Kužel, C. Kadlec, F. Kadlec, J. Schubert, and G. Panaitov, Appl. Phys. Lett. **93**, 052910 (2008).

[12] C. Kadlec, F. Kadlec, H. Němec, P. Kužel, J. Schubert, and G. Panaitov, J. Phys. Condens. Matter **21**, 115902 (2009).

[13] C. Kadlec, V. Skoromets, F. Kadlec, H. Němec, J. Hlinka, J. Schubert, G. Panaitov, and P. Kužel, Phys. Rev. B **80**, 174116 (2009).

[14] W. Chang, J. A. Bellotti, S. W. Kirchoefer, and J. M. Pond, J. Electroceram. **17**, 487 (2006).

[15] P. Kužel and F. Kadlec, C. R. Phys. **9**, 197 (2008).

[16] P. A. Fleury, J. M. Worlock, Phys. Rev. **174**, 613 (1968).

[17] F. Hecht, FreeFem++, Third Edition, Version 3.13, [http://www.freefem.org//ff++].

[18] A. Yamanaka, M. Kataoka, Y. Inaba, K. Inoue, B. Hehlen, and E. Courtens, Europhys. Lett. **50**, 688 (2000).

[19] T. Sakudo and H. Unoki, Phys. Rev. Lett. **26**, 851 (1971).

[20] P. Kužel, H. Němec, F. Kadlec, and C. Kadlec, Opt. Express **18**, 15338 (2010).

[21]H. Němec, P. Kužel, F. Kadlec, C. Kadlec, R. Yahiaoui, and P. Mounaix, Phys. Rev. B **79**, 241108(R) (2009).

[22]V. Müller, M. Rasp, G. Stefanic, J. Ba, S. Gunther, J. Rathousky, M. Niederberger, and D. Fattakhova-Rohlfing, Chem. Mater. **21**, 5229 (2009).

[23]L. Duvillaret, F. Garet, and J.-L. Coutaz, IEEE J. Sel. Top. Quantum Electron. **2**, 739 (1996).

[24]J. Hemberger, P. Lunkenheimer, R. Viana, R. Böhmer, and A. Loidl, Phys. Rev. B **52**, 13159 (1995).